Bayesian Estimation of Thermal Properties Using Periodically Pulsed Photothermal Radiometry: A Focus on Interfacial Thermal Resistances between Layers

Clément Chassain, Andrzej Kusiak, Kevin Krause, Marine Garcia, Jean-Luc Battaglia

▶ **To cite this version:**

Clément Chassain, Andrzej Kusiak, Kevin Krause, Marine Garcia, Jean-Luc Battaglia. Bayesian Estimation of Thermal Properties Using Periodically Pulsed Photothermal Radiometry: A Focus on Interfacial Thermal Resistances between Layers. physica status solidi (RRL) - Rapid Research Letters, 2022, 17 (2), pp.2200328. 10.1002/pssr.202200328 . hal-04099095

HAL Id: hal-04099095
https://hal.science/hal-04099095v1

Submitted on 16 May 2023

HAL is a multi-disciplinary open access archive for the deposit and dissemination of scientific research documents, whether they are published or not. The documents may come from teaching and research institutions in France or abroad, or from public or private research centers.

L'archive ouverte pluridisciplinaire **HAL**, est destinée au dépôt et à la diffusion de documents scientifiques de niveau recherche, publiés ou non, émanant des établissements d'enseignement et de recherche français ou étrangers, des laboratoires publics ou privés.

Bayesian Estimation of Thermal Properties Using Periodically Pulsed Photothermal Radiometry: A Focus on Interfacial Thermal Resistances between Layers

Clément Chassain, Andrzej Kusiak, Kevin Krause, Marine Garcia, and Jean-Luc Battaglia*

Pulsed periodic photothermal radiometry (PPTR) allows the investigation of multilayered samples with layer thicknesses of a few hundred nanometers over a duration of a few nanoseconds. The link between theoretical calculations and experimentation is made using a Bayesian approach based on the Metropolis–Hastings algorithm. The accuracy of the PPTR method requires precise calibration to provide an accurate proper emission measurement. Furthermore, the normalization time needs to be optimized through sensitivity analysis. Without this sensitivity analysis, it is impossible to simultaneously estimate the interfacial thermal resistances in a multilayered sample. The method is tested on multilayered samples composed of platinum (Pt), titanium nitride (TiN), silicon nitride (SiN), and silicon (Si). The parameters identified are interfacial thermal resistances between Pt–TiN and TiN–SiN.

1. Introduction

Thermal characterization of thin multilayered samples is necessary for many domains, such as electronics, thermal protection coatings, and machining tools. Many experimental techniques based on the perturbation of the sample in a homogeneous initial state have been developed.[1,2] Among them, the 3ω technique is a contact method allowing the absolute measurement of the temperature and the heat flux that is particularly well adapted to low-temperature measurements. Comparatively, contactless methods are better suited to high-temperature characterizations. The photothermal methods such as the thermoreflectance in the visible spectrum (VIS)[3–8] and infrared radiometry techniques (IR)[9–14] enable the measurement of relative variations in temperature and heat flux. This is due to the difficulty in calibrating the measurement tools and their related uncertainties. All measurement methods require a comparison between a model of the experiment and the experimental data; this comparison is the foundation of inverse methods. Inverse methods are based on optimization techniques[15,16] that aim to reduce the gap between the theoretical evaluation and the experimental measurement.

In this work, the interfacial thermal resistance is determined for an amorphous Si_3N_4 (SiN) film deposited on a silicon wafer substrate with a platinum optical-to-thermal transducer and a titanium nitride adhesive layer. In addition, the thermal conductivity for the SiN layer is identified. The experimental measurements are performed by pulsed photothermal radiometry with front-face configurations (FF-PPTR). The FF-PPTR method has been described in the literature[17] and some relevant additional information regarding the IR detector model and photothermal signal processing is provided. The Markov chain Monte Carlo (MCMC) optimization method[18–20] is used for parameter identification. One key step in the process presented in this study is the use of theoretical models from the physics of condensed matter to set the initial value of the unknown parameters. The minimal thermal conductivity model will inform a first estimate of the thermal conductivity of amorphous SiN. On the other hand, the diffuse mismatch model (DMM)[21] leads to a first estimate of the interfacial thermal resistances. Finally, the experimental signal normalization is optimized to increase the sensitivity of the sought parameters and to enhance the linear independency of their associated sensitivity funtions.

C. Chassain, A. Kusiak, K. Krause, M. Garcia, J.-L. Battaglia
I2M Laboratory
Bordeaux University
Nouvelle Aquitaine, Bordeaux 33000, France
E-mail: clement.chassain@u-bordeaux.fr

2. Experimental Section

2.1. The FF-PPTR Setup

The pulsed photothermal radiometry setup with the front-face configuration (FF-PPTR) has been described and used in previous works.[17] The setup, schematically described in **Figure 1**, was composed of a coherent,atrix Q-switch Nd:YAG diode-pumped laser (1064 nm wavelength) delivering continuous pulses with a duration of $T_s \approx 40$ ns. The repetition rate was $f_p = 1/T_r = 10$ kHz. A very small part (<2%) of the beam was sent to a fast amplified photodiode (THORLABS DET10), with 1 ns rise time, to monitor the pulse time waveform. The distance covered by the laser to reach the sample was about 0.8 m, and the beam radius at the sample surface was $r_0 = 1.75$ mm (<3 mrad divergence). Two parabolic mirrors were placed to collect the

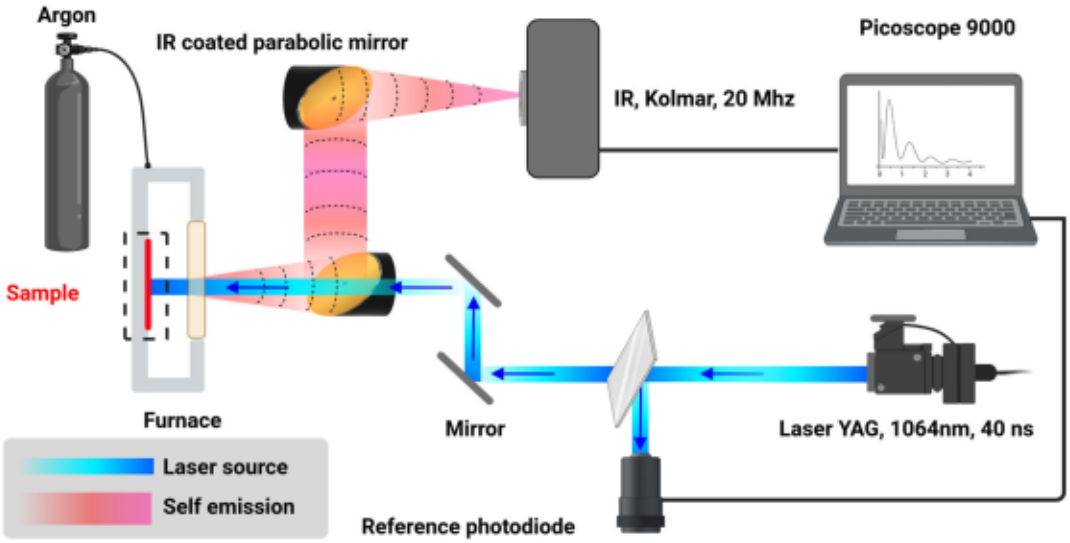

Figure 1. Experimental setup for pulsed front-end radiometry where the excitation is a sequence of N pulses repeated at the frequency $f_p = 1/T_r$.

proper emission from the heated area toward a fast photovoltaic infrared detector (Kolmar KMPV11). This sensor was composed of an integrated high-frequency HgCdTe semiconducting element working within the 2–12 µm wavelength range. This active photosensitive element was squared with edge length $A_d = 1$ mm. The signal from the IR sensor was amplified using a transimpedance amplifier working from DC up to 20 MHz. The window of the infrared detector was coated with germanium (Ge) to filter the diffused reflection of the laser and was also cooled by an external water flow system. The signals from both the photodiode and the IR detector amplifier were recorded using a Picoscope 9000 (16 bits, 50 Ω input impedance) triggered by an external source (TTL output of Agilent 33220A function generator). The sample under investigation was placed in an oven with the rear face maintained at a controlled temperature from room temperature to 800 °C. Oxidation of the sample was prevented by flowing argon gas through the oven cavity.

The IR detector and the photodiode both had a cutoff frequency and a delay. Those parameters used in a low-pass delayed filter denote F_{T_d} for the IR detector and F_{T_r} for the photodiode.

2.2. Sample Description

The sample was a stack of layers composed of a thick silicon nitride (SiN) amorphous layer deposited on a $e_{Si} = 750$ µm-thick silicon substrate. Four values of the SiN thickness were investigated, namely, e_{SiN} =[200–300] nm. To convert the laser pulse into a surface heat source, the SiN was coated with an optical-to-thermal transducer constituted of a 30 nm-thick platinum layer with an interstitial 10 nm TiN layer between Pt and SiN in order to improve the adhesion. An additional advantage of the Pt layer was to limit the oxidation and evaporation of the stack. The values reported in the literature for the thermophysical properties of the materials constitutive of the stack are given in **Figure 2**.

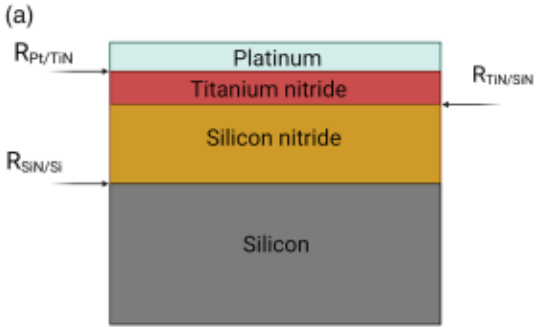

(b)

	ρ kg/m^3	Cp J/K/kg	k W/m/K	e nm
Transducer (Pt)	21350±427	130±2.6	72±1.44	30±0.6
Adhesive layer (TiN)	5210±2.6	604±12.08	29±0.58	10±0.2
Deposit (SiN)	2290±45.8	800±16	1.19±0.02	[200-500]±2
Substrate (Si)	2322±46.44	695±13.84	135±2.7	(750 ± 15).10^3

Figure 2. a) Schematic representation of the sample under investigation; b) thermophysical properties of the materials involved within the stack.[4,39–41] The standard deviations have been calculated considering 2% deviation on the parameters.

3. Mathematical Model

3.1. Impulse Response

Consider a sample as a stack of N_c contiguous layers. The radius r_0 of the heated area by the laser at the surface of the sample is larger that the expected heat penetration depth during the pulse repetition period T_r. In such a case, the heat transfer can be considered as 1D. It is also important to note that, given the very short characteristic diffusion times, heat losses by convection at the surface can be neglected. Therefore, the Laplace transform of the impulse response relating the heat flux to the surface temperature[22,23] is

$$\overline{H}(p) = \frac{A}{C} \tag{1}$$

where p is the Laplace variable. The coefficients B and D are calculated using the quadrupole method[22] as

$$\begin{bmatrix} A & B \\ C & D \end{bmatrix} = \begin{bmatrix} 1 & R_{T,1} \\ 0 & 1 \end{bmatrix} \begin{bmatrix} A_1 & B_1 \\ C_1 & D_1 \end{bmatrix} \prod_{j=2}^{N_c} \begin{bmatrix} 1 & R_{T,j} \\ 0 & 1 \end{bmatrix} \begin{bmatrix} A_j & B_j \\ C_j & D_j \end{bmatrix} \cdots \cdots \begin{bmatrix} 1 & R_{T,N_c+1} \\ 0 & 1 \end{bmatrix} \tag{2}$$

With

$$A_j = 1 + \exp(-2\gamma_i e_i);\ B_j = (1 - \exp(-2\gamma_i e_i))/\gamma_i/k_i \tag{3}$$

$$C_j = (1 - \exp(-2\gamma_i e_i))\gamma_i k_i;\ D_j = A_j \tag{4}$$

where (a_i, k_i, e_i) are, respectively, the thermal diffusivity, the thermal conductivity, and the thickness of each layer for $i = 1, N_c$ and $\gamma_i = \sqrt{p/a_i}$. The variable $R_{T,j}$ $(1 \le j \le N_c + 1)$ in Equation (2) is the interfacial thermal resistance at interface j. The resistances $R_{T,1}$ and R_{T,N_c+1} can be used to simulate resistance at the surface and between the sample and the furnace, respectively.

The relative temperature variation captured by the detector for a laser pulse is expressed as

$$\overline{\Delta T_u}(t) = \mathscr{L}^{-1}(\overline{\Delta\theta_u}(p)) \tag{5}$$

where $\mathscr{L}^{-1}()$ denotes the inverse Laplace transform. Taking into account the transfer functions F_{T_d} and F_{T_p} of the IR detector and the photodiode respectively, it is

$$\overline{\Delta\theta_u}(p) = \overline{H}(p)F_{T_s}(p)F_{T_p}(p)F_{T_d}(p) \tag{6}$$

where F_{T_s} denotes the Laplace transforms of the pulse transient waveform. The inverse Laplace transform is performed using the De Hoog algorithm.[24] Knowing the response of a single pulse, it is possible to express the response for a train of pulses (Dirac comb). Using the convolution product between Equation (5) and a Dirac comb, the following is established.

$$\overline{\Delta T}(t) = \overline{\Delta T_u}(t) * I_p(t) = \overline{\Delta T_u}(t) * \left[\sum_{n=-\infty}^{+\infty} \delta(t - nT_r)\right] \tag{7}$$

which finally results in

$$\overline{\Delta T}(t) = \sum_{0}^{M} \overline{\Delta T_u}(t + nT_r), \quad \text{for } 0 \le t \le T_r \tag{8}$$

The value of the upper limit M of the series in Equation (8) depends on the repetition frequency f_p, the thermal conductivity, and the diffusivity of the materials (specifically the substrate for the investigated configuration). Considering a Si substrate and a low repetition frequency (10 kHz), it can be shown that increasing M from 0 to 10000 leads to a change that is less than 1% in $\overline{\Delta T}(t)$. Therefore, it is worthwhile to take $M = 0$ in Equation (8) for further calculations.

3.2. Transfer Functions of the Detector and the Photodiode

According to the acquisition sampling frequency and the investigated time range of the measured signal (some hundreds of nanoseconds), the cutoff frequency f_c of the infrared detector amplifier as well as the delay τ_d of the HgCdTe photosensitive element have to be accurately measured. These two parameters are involved in the transfer function of the detector that is established as a delayed first-order low-pass filter.

$$F_{T_d}(p) = \exp(-\tau_d p)/(1 + p/2\pi f_c) \tag{9}$$

The delay τ_d is connected with the electronic band transition duration that is required for the absorbed photons to be converted in a current. On the other hand, the cutoff frequency depends mainly on the photosensitive element size. In other words, the larger the element size, the lower the cutoff frequency. The two parameters τ_d and f_c are identified by implementing the FF-PPTR on a 5 mm-thick pure tungsten (99%) pellet with diameter of 1 cm and thermal properties $k = 184\ \mathrm{W\,m^{-1}\,K^{-1}}$, $\rho = 19000\ \mathrm{kg\,m^{-3}}$, and $C_p = 130\ \mathrm{J\,K\,Kg^{-1}}$. Using the Nelder–Mead simplex method[25] to minimize the gap between the measured signal and the theoretical response from relation (8), values of $\tau_d = 23 \pm 3$ s and $f_c = 10 \pm 1$ MHz are determined. The simulated response with the identified values of τ_d and f_c is reported in **Figure 3** along with the experimental data. For information, the simulated responses based on higher values of f_c are reported in the figure. Regarding the photodiode, the transfer function of the photodiode is also a delayed low-pass filter with a cutoff frequency of 350 MHz and a delay of 1 ns. Both these parameters are given by the manufacturer.

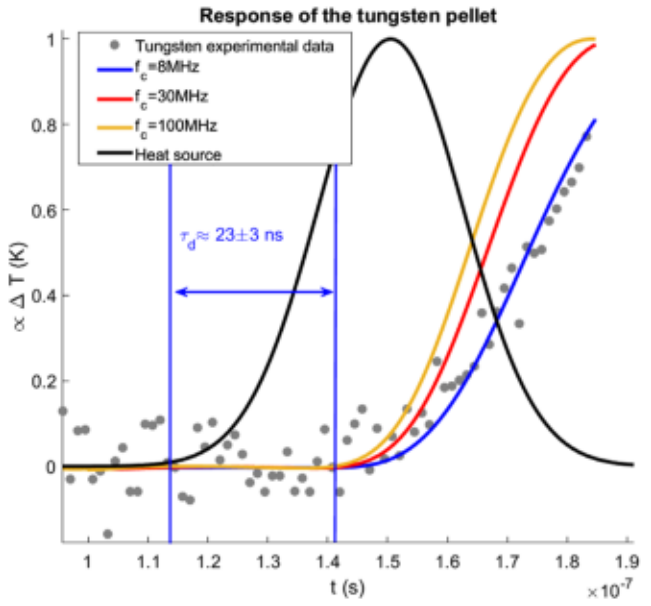

Figure 3. Measured signal when implementing the FF-PPTR on a tungsten pellet (gray dots). The simulated response from Equation (8) based on the identified values of τ_d and f_c (blue line) fits the measured data. Simulated responses based on higher values of f_c are reported in the figure for comparison (red and yellow lines).

3.3. Photothermal Pulse Waveform

The shape of the laser pulse, measured with the fast photodiode, is shown in **Figure (4)**. Clearly, the laser pulse waveform cannot be described as a Gaussian pulse. Then, to better describe the laser source time distribution, a mapping with gate functions is used. Therefore, the Laplace transform of the photothermal pulse waveform is expressed as

$$F_{T_s}(p) = \sum_j A_j(\exp(-a_{j-1}p) - \exp(-a_j p))/p \tag{10}$$

4. Parameter Identification Procedure

4.1. Normalization and Sensitivity Analysis

The target parameters are the thermal conductivity of the deposit k_{SiN}, the interface resistance $R_{Pt/TiN}$, and the interface resistance $R_{TiN/SiN}$. The interface resistance $R_{SiN/Si}$ is considered known and is allowed to vary around its theoretical values with a standard deviation of 10%.

The energy of a pulse and the quantity absorbed by the transducer is unknown; therefore, it is impossible to measure the absolute variation of temperature in an accurate way. Thus, it is essential to introduce the relative temperature variation with respect to its value at a particular time t_i. The relative temperature variation is thus expressed as

$$\overline{\Delta T}_N(t) = \frac{\overline{\Delta T}(t)}{\overline{\Delta T}(t_i)} \tag{11}$$

The maximum of $\overline{\Delta T}(t)$ is generally used as the quantity for this normalization. However, in order to be able to identify the desired experimental parameters, it is necessary that the sensitivity functions relative to each parameter are linearly independent. The sensitivity of $\overline{\Delta T}_N(t)$ to a parameter of interest $\alpha = \{k_{SiN}, R_{Pt/SiN}, R_{TiN/SiN}\}$ is calculated from the finite difference expression

$$S_\alpha^T = \alpha \frac{d\overline{\Delta T}_N(t)}{d\alpha} = \frac{\overline{\Delta T}_N(t)_{\alpha+0.1\alpha} - \overline{\Delta T}_N(t)_\alpha}{0.1} \tag{12}$$

The time t_i for the normalization will thus be chosen in order to obtain the best independence between the sensitivity functions. The sensitivity functions as well as their ratio are plotted for a 500 nm-thick deposit and a 200 nm-thick deposit in **Figure (5)** and **(6)** respectively. As shown on the figures the time chosen is crucial in order to have good sensitivity to our parameters. If the thermal response is normalized by its maximum (which is located at $t_i \approx 5.10^{-7}$ s), the sensitivity to the parameters would

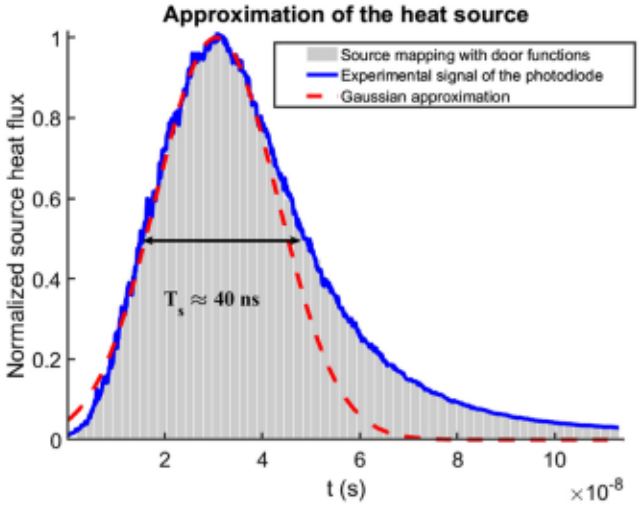

Figure 4. Laser pulse measured by the fast photodiode and the associated transfer function enable a simple inverse Laplace transform calculation.

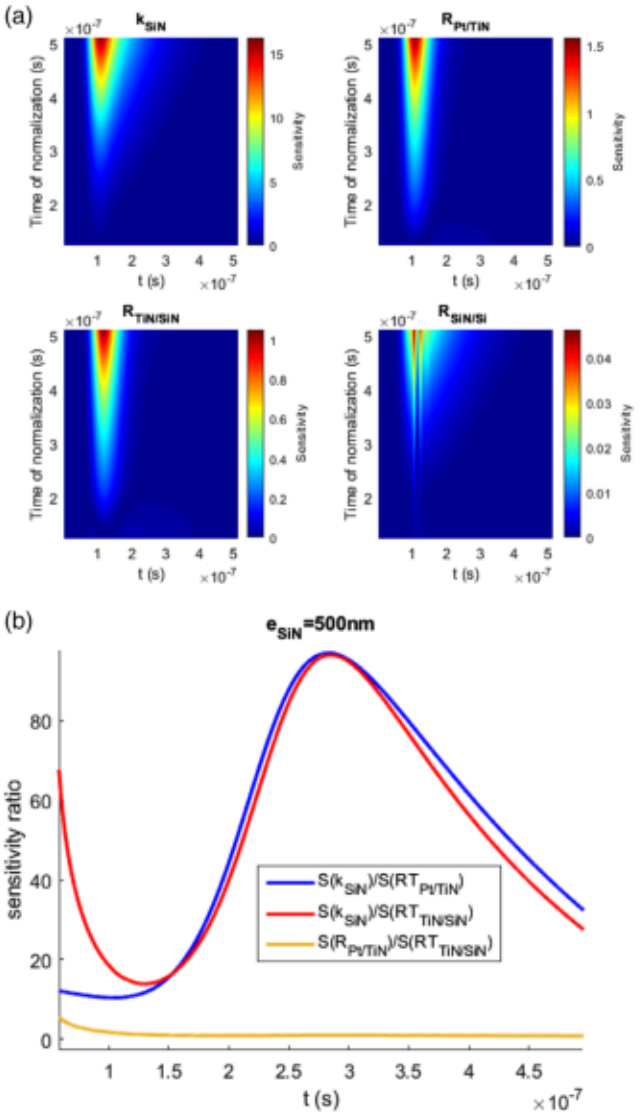

Figure 5. a) Sensitivities to the conductivity k_{SiN} of the 500 nm-thick deposit, to the first interface resistance $R_{Pt/TiN}$, to the second interface resistance $R_{TiN/SiN}$, and to the third interface resistance $R_{SiN/Si}$ calculated from the values Table (1) and Equation (8). b) Ratio of the sensitivity functions for a 500 nm-thick deposit for t_i 5×10^{-7} s.

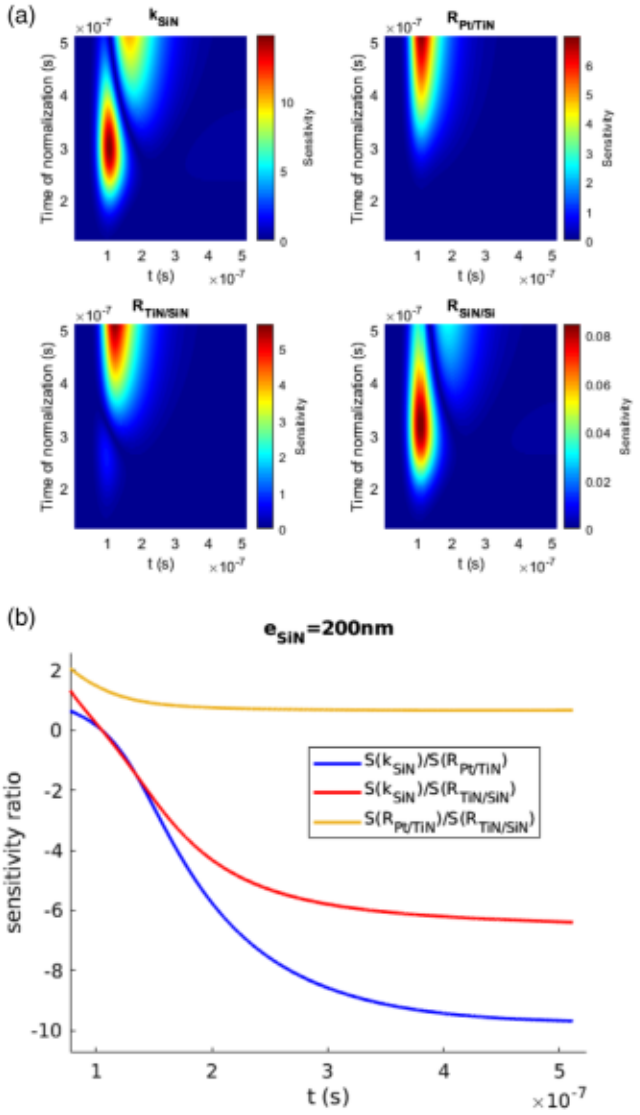

Figure 6. a) Sensitivities to the conductivity k_{SiN} of the 200 nm-thick deposit, to the first interface resistance $R_{Pt/TiN}$, to the second interface resistance $R_{TiN/SiN}$, and to the third interface resistance $R_{SiN/Si}$ calculated from the values in Table (2) and Equation (8). b) Ratio of the sensitivity functions for a 200 nm-thick deposit for t_i 3×10^{-7} s.

be greatly reduced and almost negated in certain cases. Even more important, choosing a suited normalization time can help to reduce the linear dependency of the sensitivity functions between the parameters. The effect of the normalization on the ratio of the sensitivity functions is shown in Equation (12).

$$\frac{S^T_{\alpha_1}}{S^T_{\alpha_2}} = \frac{\frac{\partial}{\partial\alpha_1}(\Delta T(t,\alpha_1,\alpha_2))\Delta T(t_i,\alpha_1,\alpha_2) - \cdots}{\frac{\partial}{\partial\alpha_2}(\Delta T(t,\alpha_1,\alpha_2))\Delta T(t_i,\alpha_1,\alpha_2) - \cdots} \frac{\cdots \Delta T(t,\alpha_1,\alpha_2)\frac{\partial}{\partial\alpha_1}(\Delta T(t_i,\alpha_1,\alpha_2))}{\cdots \Delta T(t,\alpha_1,\alpha_2)\frac{\partial}{\partial\alpha_2}(\Delta T(t_i,\alpha_1,\alpha_2))} \tag{13}$$

Figure (5) and (6) also show that t_i varies regarding the thickness of the deposit, which means that for every thickness this sensitivity analysis needs to be conducted in order to optimize the identification of the parameters.

4.2. Expected Values from Theoretical Physics

The theoretical thermal conductivity of the amorphous SiN can be calculated using the minimal thermal conductivity model.[26] The interfacial thermal resistances can also be calculated from the DMM.[21] Those theoretical results will be used as initial and prior values within the MCMC method. Since those theoretical values are expected to be quite close to the true values, the implementation of the delayed rejection adaptive metropolis (DRAM) algorithm is proposed for faster computation than the Metropolis–Hastings algorithm.

4.3. The Diffuse Mismatch Model (DMM)

The DMM[21] is used to calculate the value of interfacial thermal resistance at a perfect interface between two layers. This model is suitable with the diffuse scattering of phonons at both sides of the interface when temperature is high enough. Considering that the thermal equilibrium and the transmission of the phonon through the interface is not dependent on the incidence angle, then it is possible to express the interfacial thermal resistance between the layer 1 and the layer 2 as

$$R_{1\to2} = \left(\sum_j \frac{k_B^4 T^3}{8\pi^2\hbar^3 v_{j,1}^2}\alpha_{1\to2}\int_0^{\Theta_{D,1}/T}\frac{x^4 e^x}{(e^x-1)^2}\mathrm{d}x\right)^{-1} \tag{14}$$

where k_B is the Boltzmann constant and T is the temperature. The change of variable $x = \hbar\omega/k_B T$ has been realized and the Debye temperature is expressed as $\Theta_D = \hbar\omega_m/k_B$. Moreover, v_j (with $j = (L, T, T)$) is the velocity of the phonons in different directions, L is the longitudinal direction, and T are the two transverse ones. The transmission coefficient α is defined in such a case as

$$\alpha_{1\to2} = \frac{v_{L,2}^{-2} + 2v_{T,2}^{-2}}{v_{L,1}^{-2} + 2v_{T,1}^{-2} + v_{L,2}^{-2} + 2v_{T,2}^{-2}} \tag{15}$$

As said previously, this calculated value assumes perfect interface with perfect adhesion between the two layers. It means that bad chemical adhesion, delamination, or rugosities are not considered with the DMM model. It has been shown that the contribution of anharmonic processes can be non-negligible.[27] Thus the DMM computations can diverge greatly from the experimental values. The parameters used for the computations are reported in **Table** (1) and the results of the DMM calculations are reported in **Table** (2).

4.4. Minimum Thermal Conductivity

The thermal conductivity can be calculated from the Boltzmann transport equations (BTE)[28] assuming Debye approximation.[29–32] Considering the phonon velocity v_i for the branches i and the Debye

Table 1. Parameters used for the DMM,[42–45] V_T is the transverse phonon velocity, V_L is the longitudinal phonon velocity, and Θ_D is the Debye temperature.

	V_L [m s^{-1}]	V_T [m s^{-1}]	V_T [m s^{-1}]	Θ_D [K]
Pt	4174	1750	1750	225
TiN	10221	5110	5110	580
Si_3N_4	9100	5200	5200	637
Si	8480	5860	5860	692

Table 2. Results of the DMM. The standard deviations have been calculated considering a 10% deviation on the phonon velocities.

$R_{Pt/TiN}$ [m^{2}K W^{-1}]	$R_{TiN/SiN}$ [m^{2}K W^{-1}]	$R_{SiN/Si}$ [m^{2}K W^{-1}]
$(1.73 \pm 0.04) \times 10^{-8}$	$(2.16 \pm 0.22) \times 10^{-9}$	$(1.74 \pm 0.05) \times 10^{-9}$

temperature $\Theta_{D,i} = v_i(\hbar/k_B)(6\pi^2 n)^{1/3}$, Cahill and Pohl[26] proposed an expression for the minimum thermal conductivity.

$$k_{min} = \left(\frac{\pi}{6}\right)^{1/3} k_B N^{2/3} \sum_{i=1}^{3} v_i \left(\frac{T}{\Theta_i}\right)^2 \int_0^{\Theta_{D,i}/T} \frac{x^3 e^x}{(e^x - 1)^2} dx \quad (16)$$

with the change of variable $x = \hbar\omega/k_B T$. For the amorphous SiN layer, it is found $k_{min_{SiN}} = 1.19 \pm 0.13$ W m^{-1} K^{-1}, the parameters used for the phonon velocities and the Debye temperature reported in Table 1 and with the density that is $\rho_{SiN} = 2290$ kg m^{-3}. It has been shown that the mean free path of phonon masters the thermal transport within the bulk for dielectrics.[33] It has also been shown that, for phonons having a mean free path greater than the thickness of the medium they propagate through, phonon wave localization can happen[34] thus, lowering the thermal conductivity of the material. This means that for low temperatures and low film thicknesses, the experimental value can greatly diverge from the theoretical one. In such cases, another computation of the initial guess may be better suited.

4.5. The Markov Chain Monte Carlo Method (MCMC)

The DMM and the BTE calculations are coupled to a Bayesian approach such as the MCMC method, precisely the Metropolis–Hastings algorithm.[18–20] The theoretical calculations are used as starting points for the minimization method and will be used for the prior information such as the lower and upper bounds that the parameters can take as well as their variance.

The Monte Carlo method is based on two foundations, the law of large numbers and the central limit theorem. The first of these two theorems expresses the fact of having a large number of samples from a distribution of random variables, and then the average of these samples provides the expected value. The second one informs that a sum of identical and independent random variables trends towards a random variable with normal distribution, which also means that the confidence intervals can be calculated. The Metropolis–Hastings algorithm comes into play as a sampler of the random variables X_n while offering a Bayesian inference to their sampling. The steps of the algorithm can be listed as follows: 1) Define starting points P_1 for the parameters you seek; 2) Sample a candidate P^* from a candidate proposal distribution $q(P^*|P_n)$; 3) Compute the ratio of the posterior probability densities. $\alpha(P^*|P_n) = \frac{\pi(Y|P^*)\pi(P^*)q(P_n|P^*)}{\pi(Y|P_n)\pi(P_n)q(P^*|P_n)}$; 4) Generate a random value $U \approx U(0,1)$, which is uniformly distributed in (0,1); 5) If $U \leq \alpha(P^*|P_n)$, set $P_{n+1} = P^*$; 6) If $U > \alpha(P^*|P_n)$, set $P_{n+1} = P_n$; and 7) Return to step 2.

The proposal distribution $q(P_n|P^*)$ is arbitrarily chosen for each parameter, it follows a normal distribution with a mean equal as the value of the current candidate P and a standard deviation corresponding to 5% of its actual value. The a priori probability density $\pi(P)$ is a normal distribution with upper and lower bounds' set $[A; B]$ arbitrarily, with a mean μ determined by DMM and BTE and with a standard deviation σ corresponding to 10% of its mean. The likelihood distribution $\pi(Y|P)$ is a distribution directly proportional to the squared error between the measurements and our model.

Since decreasing the thickness of the deposit increases the correlation between sensitivity function, priors for the lowest

Table 3. Parameters used for the a priori normal distributions in the MCMC method for the 500 nm-thick deposit. A and B are the sampling boundaries, μ is the mean, and σ is the standard deviation.

	A	B	μ	σ
$\pi(k_{SiN})$	$-\infty$	$+\infty$	0	$+\infty$
$\pi(R_{Pt/TiN})$	$-\infty$	$+\infty$	0	$+\infty$
$\pi(R_{TiN/SiN})$	$-\infty$	$+\infty$	0	$+\infty$
$\pi(R_{SiN/Si})$	$-\infty$	$+\infty$	1.74e−9	1.74e−10

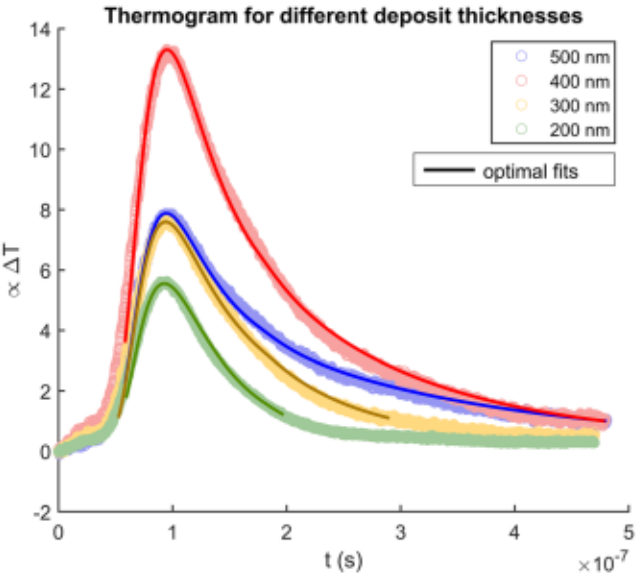

Figure 7. Experimental measurements of multilayered samples by pulsed photothermal radiometry for Si_3N_4 deposits of different thicknesses. The model plot with the optimal parameter values found by MCMC is also reported.

deposit thicknesses will be established based on the results of the identification of the parameters on the 500 nm-thick deposit sample. The parameters used to identify the properties of the 500 nm-thick deposit sample via MCMC are reported in **Table (3)**.

To improve the efficiency of the resulting MCMC estimates, the DRAM,[35] which is a combination of the delayed rejection (DR)[36] and the adaptive metropolis (AM) algorithm,[37] is used. The DR allows that upon rejection, instead of advancing to the next iteration and retaining the current position, a second stage move is proposed. To propose a second candidate, the first candidate proposal distribution is scaled down (reducing the standard deviation of the said distribution). The second candidate is accepted if the sample from $U(0,1)$ is inferior to the probability α_{i+1}.

Table 4. Experimental parameters identified by the MCMC method using the Metropolis–Hastings algorithm. The parameters are derived from the average of all samples drawn by MCMC.

	k_{SiN} [W m^{-1}K^{-1}]	$R_{Pt/TiN}$ [m^{2}K W^{-1}]	$R_{TiN/SiN}$ [m^{2}K W^{-1}]	$R_{SiN/Si}$ [m^{2}K W^{-1}]
500	1.12 ± 0.02	$(7.80 \pm 1.20).10^{-8}$	$(4.01 \pm 1.69) \times 10^{-8}$	1.74×10^{-9}
400	1.18 ± 0.01	$(10.08 \pm 0.69).10^{-8}$	$(3.86 \pm 0.78) \times 10^{-8}$	1.74×10^{-9}
300	1.19 ± 0.01	$(10.61 \pm 0.69).10^{-8}$	$(2.65 \pm 0.67) \times 10^{-8}$	1.73×10^{-9}
200	1.45 ± 0.02	$(9.1 \pm 0.93).10^{-8}$	$(3.65 \pm 0.40) \times 10^{-8}$	1.73×10^{-9}

$$\alpha_{i+1}(P^{**}|P_n, P^*) = \frac{\pi(Y|P^{**})\pi(P^{**})q_i(P^*|P^{**})}{\pi(Y|P_n)\pi(P_n)q_i(P^*|P_n)} \cdots \cdots \frac{q_{i+1}(P^{**}|P^*, P_n)[1-\alpha_i(P^*|P^{**})]}{q_{i+1}(P^{**}|P_n, P^*)[1-\alpha_i(P^*|P_n)]} \tag{17}$$

Three possible additional stages are used, one where q is down-scaled by a factor of 5, then by 4, and then by 3. It is possible to repeat until satisfactory or upscale the candidate proposal distribution instead of downscaling. The AM is used to change the standard deviation of the candidate proposal distribution of each parameter based on how the Markov chain behaves. Every N iteration, the standard deviation of q is replaced by the standard deviation from the last N samples of the chain.

$$\sigma_N = = \begin{cases} \sigma_{\text{ini}}, \text{ for } n < N \\ s_d * \sigma(X_0, X_1 \ldots X_N) + s_d I_d, \text{ for } n > N \end{cases} \tag{18}$$

Here I_d denotes the d-dimensional identity matrix. The parameter s_d only depends on the dimension d of the state space and is chosen such as $s_d = (2.4)^2/d$.[38] There are numerous ways to combine DR and AM into DRAM; in this work, the candidate proposal distribution is first modified according to AM and then the DR is applied.

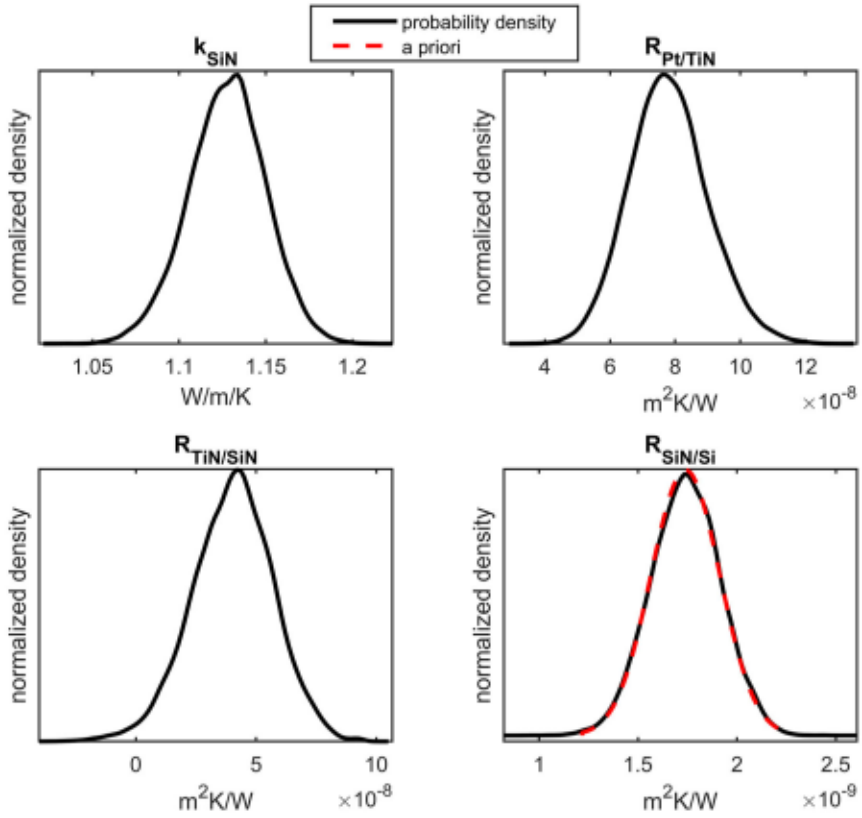

Figure 8. Optimal parameters identified for 30000 iterations from the MCMC method with the Metropolis–Hastings algorithm for a Si_3N_4 deposit with thickness of 500 nm. The model plot from these optimal parameters and the parameters in Table 4 are plotted Figure 7. The values for all the thicknesses are reported Table 4.

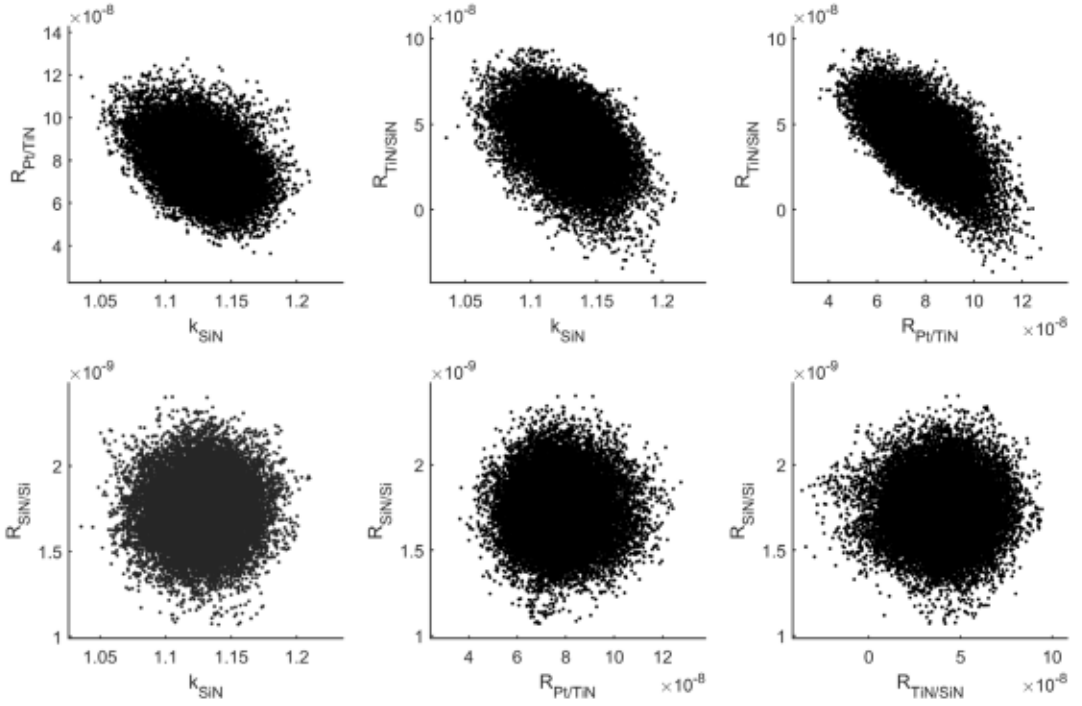

Figure 9. Markov chains for 30000 iterations from the MCMC method with the Metropolis-Hastings algorithm for Si_3N_4 deposit with thickness of 500 nm.

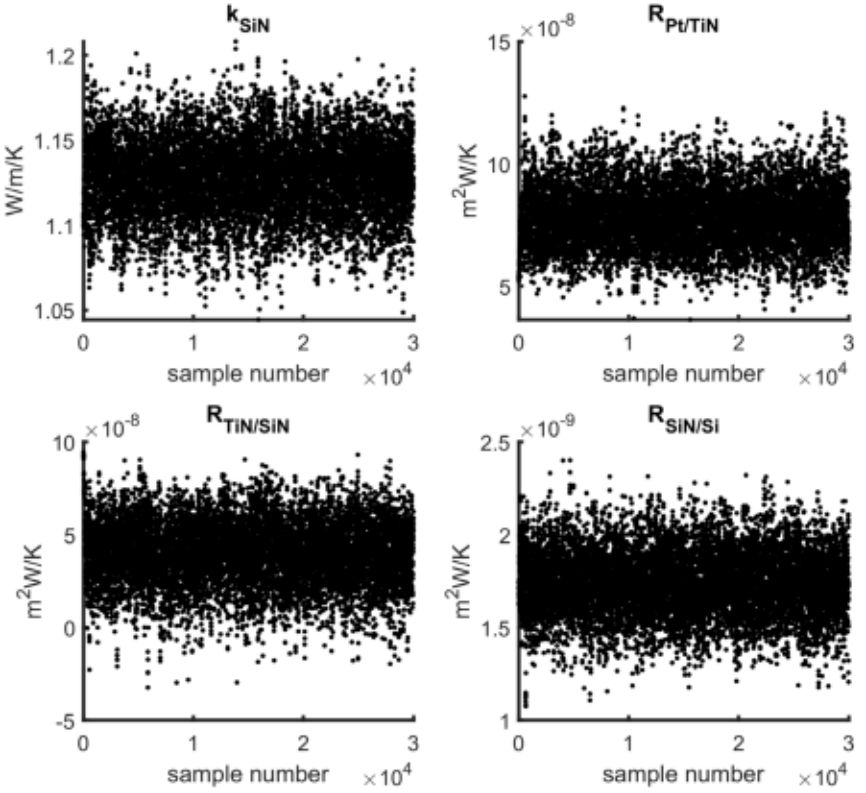

Figure 10. Pairwise scatter plots for 30000 iterations from the MCMC method with the Metropolis-Hastings algorithm for Si_3N_4 deposit thickness of 500 nm.

5. Results

The study was performed on the four deposition thicknesses and with 30000 iterations each for the Metropolis–Hastings algorithm. The identified optimal parameters that were used for the model are plotted in **Figure** (**7**) and reported in **Table** (**4**). The repartitions of the samples drawn during the algorithm are shown **Figure** ((**8**). The Markov chains and the pairwise scatter plots are displayed in **Figure** (**9**) and in (**10**) respectively. The convergence of the algorithm is shown, thanks to the steady state of the Markov chains. It is also shown on the pairwise scatterplots that the parameters have no influence on each other since the shape they describe follows no linear trend.

Considering the weighted average of the results over all the sample thicknesses leads to $k_{SiN} = 1.23 \pm 0.16\,W\,m^{-1}\,K^{-1}$, $R_{Pt/TiN} = (9.66 \pm 1.23) \times 10^{-8}\,m^2\,K\,W^{-1}$, and $R_{TiN/SiN} = (3.47 \pm 0.61) \times 10^{-8}\,m^2\,K\,W^{-1}$. The thermal conductivity of the SiN is close to the theoretical value since the model developed by Cahil and Pohl is accurate for high density and fully amorphous materials, which is the case of the SiN. As expected, the first resistance $R_{Pt/TiN}$ has a higher estimated value than the one computed because of weak chemical adhesion; that is not taken into account in the DMM. Regarding the second resistance $R_{TiN/SiN}$, the high estimated value of this parameter compared to the theoretical one may be attributed to the crystalline phase hypothesis used for the DMM computations. In fact, the DMM assumes a crystalline arrangement which is not the case for SiN. In such a case, the phonons going through the interface will greatly slow down, leading to an increase of the interfacial thermal resistance. The average values of the samples drawn by MCMC for the parameters are shown in Table (4).

6. Conclusion

In this articles, we were able to show that periodic pulsed photothermal radiometry is a reliable method for investigating the physical properties of thin multilayered samples. It has been shown that considering all influencing factors, such as the transfer function of the detector and the source, is important for the accuracy of the method. In addition, a robust technical solution to the identification of the first interface resistance is presented by coupling with theoretical calculations, such as the DMM and the minimum thermal conductivity model, to the DRAM MCMC optimization method. The method has been illustrated on four samples of different thicknesses where the results all converge to the same values and are in agreement with other measurements, the literature or the theoretical values. It was also shown that the sensitivity analysis regarding the normalization time is key for an optimal identification of the parameters. In fact, by choosing an adequate normalization time we were able to reduce the linear dependence of the sensitivity functions, allowing us to identify three parameters at once. This strong result might be an important tool in the domain of inverse methods, especially in thermal science, where it may be possible to reduce the ill-posed character of the problems we face.

Moreover, with a sensor having a higher cut-off frequency and taking into account the future progress of the instrumentation, it is very likely that in the future we will be able to obtain valuable information delivered by thermal diffusion at very short times with greatly increased accuracy.

Acknowledgements

This project received funding from the European Union Horizon 2020 research and innovation program under grant agreement no. 824957 (BeforeHand: Boosting Perfor- mance of Phase Change Devices by Hetero- and Nanostruc- ture Material Design).

Conflict of Interest

The authors declare no conflict of interest.

Data Availability Statement

The data that support the findings of this study are available from the corresponding author upon reasonable request.

Keywords

interfacial thermal resistances, inverse methods, Markov chain Monte Carlo, multilayered, nanoscales, normalization methods

Received: August 31, 2022
Revised: October 14, 2022
Published online: November 8, 2022

[1] D. G. Cahill, *Rev. Sci. Instrum.* **1990**, *61*, 802.
[2] C. E. Raudzis, F. Schatz, D. Wharam, *J. Appl. Phys.* **2003**, *93*, 6050.
[3] D. G. Cahill, *Rev. Sci. Instrum.* **2004**, *75*, 5119.
[4] T. Baba, K. Ishikawa, T. Yagi, N. Taketoshi, (preprint) arXiv:0709.1845, final version, submitted: Sept. 2007.
[5] P. L. Komarov, M. G. Burzo, and P. E. Raad, in *Twenty-Second Annual IEEE Semicon-ductor Thermal Measurement And Management Symposium*, IEEE, Piscataway, NJ, **2006**, pp. 199–203.
[6] W. S. Capinski, H. J. Maris, *Rev. Sci. Instrum.* **1996**, *67*, 2720.
[7] N. Taketoshi, T. Baba, E. Schaub, A. Ono, *Rev. Sci. Instrum.* **2003**, *74*, 5226.
[8] S. Dilhaire, G. Pernot, G. Calbris, J.-M. Rampnoux, S. Grauby, *J. Appl. Phys.* **2011**, *110*, 114314.
[9] M. Depriester, P. Hus, S. Delenclos, A. Hadj Sahraoui, *Rev. Sci. Instrum.* **2005**, *76*, 074902.
[10] A. Salazar, A. Oleaga, A. Mendioroz, E. Apiñaniz, *Measurement* **2018**, *121*, 96.
[11] P.-E. Nordal, S. O. Kanstad, *Phys. Scr.* **1979**, *20*, 659.
[12] S. Andre, B. Remy, D. Maillet, A. Degiovanni, J.-J. Serra, *J. Appl. Phys.* **2004**, *96*, 2566.
[13] J.-L. Battaglia, A. Kusiak, M. Bamford, J.-C. Batsale, *Int. J. Therm. Sci.* **2006**, *45*, 1035.
[14] N. Horny, M. Chirtoc, A. Fleming, G. Hamaoui, H. Ban, *Appl. Phys. Lett.* **2016**, *109*, 033103.
[15] J. V. Beck, K. J. Arnold, *Parameter Estimation in Engineering and Science*, Wiley **1977**.
[16] R. C. Aster, B. Borchers, C. H. Thurber, *Parameter Estimation and Inverse Problems*, Elsevier **2018**.
[17] J.-L. Battaglia, E. Ruffo, A. Kusiak, C. Pradere, E. Abisset, S. Chevalier, A. Sommier, J.-C. Batsale, *Measurement* **2020**, *158*, 107691.
[18] W. K. Hastings, *Biometrika* **1970**, *57*, 97.

[19] J. P. Kaipio, C. Fox, *Heat Transfer Eng.* **2011**, *32*, 718.
[20] H. R. B. Orlande, G. S. Dulikravich, M. Neumayer, D. Watzenig, M. J. Colaço, *Numer. Heat Transfer, Part A* **2014**, *65*, 1.
[21] E. T. Swartz, R. O. Pohl, *Rev. Mod. Phys.* **1989**, *61*, 605.
[22] D. Maillet, S. Andre. J. Batsale, A. Degiovanni, C. Moyne, *Thermal Quadrupoles*, Wiley **2000**.
[23] A. Degiovanni, C. Pradere, E. Ruffio, J.-L. Battaglia, *Int. J. Therm. Sci.* **2018**, *130*, 518.
[24] F. R. de Hoog, J. H. Knight, A. N. Stokes, *SIAM J. Sci. Stat. Comput.* **1982**, *3*, 357.
[25] J. A. Nelder, R. Mead, *Comput. J.* **1965**, *7*, 308.
[26] D. G. Cahill, S. K. Watson, R. O. Pohl, *Phys. Rev. B* **1992**, *46*, 6131.
[27] D. Ma, Y. Zhao, L. Zhang, *J. Appl. Phys.* **2021**, *129*, 175302.
[28] P. Sybil, *McGraw-Hill Encyclopedia of Physics*, McGraw-Hill **1993**.
[29] P. Debye, *Ann. Phys.* **1912**, *344*, 789.
[30] C. Kittel, P. McEuen, P. McEuen. *Introduction to Solid State Physics*, Vol. *8*. Wiley, New York, **1996**.
[31] D. V. Schroeder, *Am. J. Phys.* **1999**, *67*, 1284.
[32] J. Callaway, H. C. von Baeyer, *Phys. Rev.* **1960**, *120*, 1149.
[33] J. M. Larkin, A. J. H. McGaughey, *Phys. Rev. B* **2014**, *89*, 144303.
[34] R. Hu, S. Iwamoto, L. Feng, S. Ju, S. Hu, M. Ohnishi, N. Nagai, K. Hirakawa, J. Shiomi, *Phys. Rev. X* **2020**, *10*, 021050.
[35] H. Haario, M. Laine, A. Mira, E. Saksman, *Stat. Comput.* **2006**, *16*, 339.
[36] A. Mira, *Metron* **2001**, *59*, 231.
[37] H. Haario, E. Saksman, J. Tamminen, *Bernoulli* **2001**, *7*, 223.
[38] A. Gelman, G. O. Roberts, W. R. Gilks, *Bayesian Stat.* **1996**, *5*, 42.
[39] H. Ftouni, C. Blanc, D. Tainoff, A. D. Fefferman, M. Defoort, K. J. Lulla, J. Richard, E. Collin, O. Bourgeois, *Phys. Rev. B* **2015**, *92*, 125439.
[40] M. W. Chase, National Information Standards Organization (US), *NIST-JANAF Thermochemical Tables*, Vol. *9*, American Chemical Society, Washington, DC **1998**
[41] W. M. Haynes, D. R. Lide, T. J. Bruno, *CRC Handbook of Chemistry and Physics*, CRC Press, Boca Raton **2016**.
[42] D. Lacroix, I. Traore, S. Fumeron, G. Jeandel, *Eur. Phys. J. B* **2009**, *67*, 15.
[43] A. K. Kushwaha, *NISCAIR-CSIR* **2015**, 585, http://nopr.niscpr.res.in/handle/123456789/32125.
[44] J. F. Shackelford, W. Alexander, *CRC Materials Science and Engineering Handbook*, CRC Press, Boca Raton **2000**.
[45] S. A. Baily, D. Emin, H. Li, *Solid State Commun.* **2006**, *139*, 161.